A&A 391, 1081–1095 (2002)
DOI: 10.1051/0004-6361:20020864

Astronomy & Astrophysics

The physical structure of Magellanic Cloud H II regions

II. Elemental abundances

R. Vermeij and J. M. van der Hulst

Kapteyn Astronomical Institute, PO Box 800, 9700 AV Groningen, The Netherlands

Received 17 April 2002 / Accepted 6 June 2002

Abstract. Based on a new data set of optical and infrared spectra described in Vermeij et al. (2001), we analyse the gas-phase elemental abundances of a sample of H II regions in the Large and Small Magellanic Cloud. The combined optical and infrared data set gives us access to all the ionization stages of astrophysically important elements such as sulfur and oxygen. We self-consistently determine the electron temperatures and densities for the O^+, S^{++} and O^{++} ionization zones, and use these parameters in the derivation of the ionic fractions. We discuss the uncertainties on these ionic fractions. The different relations between the electron temperatures as proposed by Garnett (1992) and Thuan et al. (1995) are confronted with our results. We find our electron temperatures to be consistent with these relations, although the relation between T_e [S III] and T_e [O III] might be slightly steeper than predicted. We investigate the reliability of the Ionization Correction Factors (ICFs) used in the derivation of the full elemental abundances of sulfur and neon. We conclude that the prescription for the ICF used to derive the sulfur abundance as given by Stasińska (1978) for $\alpha = 3$ is accurate for $O^+/O > 0.20$. No conclusions could be drawn for neon. Avoiding the use of ICFs as much as possible, we then proceed to derive the full elemental abundances. We calculate a grid of general photoionization models to compare our results with the "bright-line" abundance diagnostics for oxygen (R23) and sulfur (S23(4)). The reliability of the newly proposed S234 parameter (Oey & Shields 2000) which includes emission lines from S^+, S^{++} and S^{+3} is checked. We find a very good agreement between the S234 models and our analysis results. Finally, we compare the heavy element-to-oxygen ratios of our sample objects to those of giant H II regions in a large sample of low-metallicity blue dwarf galaxies (Izotov & Thuan 1999) and with the results from Kobulnicky & Skillman (1996, 1997) for the irregular galaxies NGC 1569 and NGC 4214.

Key words. ISM: structure, abundances – ISM: lines and bands – H II regions – Magellanic Clouds

1. Introduction

Because of their often very rich emission-line spectra, astrophysical plasmas are an important tool for studying the gas-phase interstellar medium (ISM). Starforming or H II regions are therefore well suited for deriving the properties of the ISM. These properties include the density and temperature of the ionized plasma, but, more importantly, also the gas-phase elemental abundances. Knowledge of the chemical composition of the ISM provides an important constraint on the star formation history and chemical evolution of a galaxy and should therefore be accurately known (e.g. Russell & Dopita 1992; Tsujimoto et al. 1995; Pagel & Tautvaišienė 1998).

An important prerequisite for the correct derivation of abundances is a good determination of the electron density and temperature. Of these two, the temperature is the most crucial. The electron temperature that has traditionaly been used for deriving abundances is the one derived from the optical lines of O^{++}, but this simple approach of assuming one and the same temperature for every element is oversimplified. Any good derivation of elemental abundances should take into account that different ionic species, residing in their own ionization zone, can have their own electron temperature (Garnett 1992), and that these temperatures can be biased towards higher values because of small-scale temperature fluctuations (Peimbert 1967). Failing to do so can lead to serious errors in the derived abundandes.

The reliability of the derived elemental abundances is also compromised by the fact that not every ionic stage of an element has suitable emission lines to derive an ionic fraction from. Not taking into account these unseen ionization stages leads to an underestimate of the total abundance. The usual way to "remedy" this problem is by the use of Ionization Correction Factors (ICFs). Many descriptions of these ICFs have appeared for the different elements, either based on coincidences in the atomic properties of the various ionic species involved (e.g. Peimbert & Costero 1969) or on photoionization models (e.g. Stasińska 1978). The proper correction for the missing ionization stages to make, however, is not always clear and has proven to be difficult for important elements such as sulfur (Natta et al. 1980; Dennefeld & Stasińska 1983).

Both these problems can be alleviated, if not solved, by extending the usual optical data base into the infrared. The inclusion of the fine-structure lines in the infrared makes it possible

Send offprint requests to: R. Vermeij,
e-mail: ronald@astro.rug.nl

Table 1. The electron temperatures (K) and densities (cm^{-3}) of the O^{++}, S^{++} and O^{+} zones. The temperatures were all derived from optical spectra. The O^{++} and S^{++} electron densities were derived from ratios of infrared lines, whereas the S^{+} densities are based on optical longslit spectra. The uncertainties in the derived parameters are included in parentheses.

#	Object	T_e [O III]	n_e [O III]	T_e [S III]	n_e [S III]	T_e [O II]	n_e [S II]
1	N81	13 320 (170)	140 (100)	13 960 (1150)	750 (650)	11 900 (1800)	400 (90)
2	N88A	14 990 (240)	1960 (700)	14 830 (1170)	2200 (1750)	11 000 (2200)	1620 (270)
3	N66	12 300 (500)	–	13 750 (2800)	–	11 980 (1000)	500†
4	N79A	10 640 (700)	–	9000 (1000)	–	11 200 (1000)	500†
5	N4A	10 100 (290)	150 (30)	9800 (700)	360 (300)	11 700 (2000)	220 (120)
6	N83B	11 270 (700)	150 (30)	9800 (1000)	620 (500)	16 610 (6300)	680 (170)
7	N11A	9690 (200)	–	10 400 (1400)	750 (600)	10 990 (2090)	370 (70)
8	N159-5	11 300 (900)	120 (20)	8000 (1500)	270 (160)	10 600 (2800)	370 (210)
9	N157B	13 500 (1300)	–	9600 (1200)	200 (200)	–	500†
10	30 Dor#1	10 990 (600)	170 (20)	10 470 (1500)	–	–	500†
11	30 Dor#2	10 640 (500)	190 (20)	10 730 (1900)	190 (190)	10 180 (1100)⋆	460 (120)⋆
12	30 Dor#3	10 570 (500)	190 (20)	9970 (1000)	–	11 640 (1340)⋆	570 (120)⋆
13	30 Dor#4	10 970 (500)	150 (30)	10 860 (1600)	–	11 200 (1320)⋆	400 (100)⋆
14	N160A1	9970 (200)	220 (30)‡	9230 (600)	450 (400)	10 200 (1600)	610 (120)
15	N160A2	9710 (180)	220 (30)‡	9140 (600)	620 (500)	10 000 (1600)	660 (130)

† Adopted value. ‡ The objects fall within the LWS beam simultaneously.
⋆ Derived from longslit spectra from Vermeij & van der Hulst, in preparation.

to derive plasma properties for more different ionization zones, giving a better coverage of the temperature and density profile of the nebula. The larger spectral coverage also gives us access to more different, otherwise unobservable, ionic species which makes a direct calculation of the elemental abundance possible without having to resort to ICFs. The *Infrared Space Observatory* (ISO, Kessler et al. 1996) has now opened up this infrared window and has allowed us to combine the optical and infrared spectral regimes.

Using a new data base of infrared and optical spectroscopical data described in Vermeij et al. (2001) (Paper I), we re-examine the elemental abundances of a sample of H II regions in the Magellanic Clouds. We use the H II regions in our sample primarily in their role as probe of the local gas-phase abundances, but we also address their large-scale temperature stratification. The paper is organized as follows. A short description of the data used in this work is given in Sect. 2. In Sect. 3 the analysis in terms of electron gas properties and abundances is presented. A discussion on the derived electron gas properties with emphasis on the large-scale temperature stratification is given in Sect. 4. Also given in this section is a discussion on the reliability of the derived ionic fractions and total abundances, and on the ionization correction factors used to derive these. In Sect. 5, we take a look at the different "bright line" methods for deriving abundances, and in Sect. 6 we briefly discuss the nucleosynthetic aspects. Section 7 gives a summary.

2. Data set

The data set used in the analysis presented here is described in a previous paper (Vermeij et al. 2001, Paper I), in which a detailed account of the reduction process as well as a discussion regarding the reliability and the quality of the data can be found. Here we will only give a short summary of the most relevant points.

The data set consists of two parts. The first part is made up of a large set of optical driftscan and stationary longslit spectra. These were obtained in December 1995 and December 1996 with the Boller & Chivens spectrograph on the ESO 1.52 meter telescope. The optical spectra cover various spectral ranges, varying from 2880 Å to 11 150 Å and from 3977 Å to 9780 Å. All spectra include the [O III] 4363 Å, [S III] 6312 Åand [O II] (7320 + 7330) Å lines important for deriving electron temperatures. Also included are the [S III] 9068 Å and [S III] 9532 Å lines. An assessment of the impact of telluric absorption on these latter two lines was made.

The optical data are complemented by infrared spectra obtained with the *Short Wavelength Spectrometer* (SWS, de Graauw et al. 1996) and *Long Wavelength Spectrometer* (LWS, Clegg et al. 1996) on board the Infrared Space Observatory (ISO) as part of a Guaranteed Time Program of H II regions in Local Group Galaxies. The SWS data were obtained using mainly the AOT2 line-scanning mode. The infrared lines observed include amongst others the [Ne II] 12.8 μm, [S IV] 10.5 μm, [Ne III] 15.6 μm, [S III] 18.7 μm and [O III] 52 μm lines.

3. Analysis

For the analysis involving the fine-structure lines, a five-level atom was used as a model. The relative populations of the five levels were calculated by taking into account the (de)population mechanisms of collisonal excitation and de-excitation by electrons, and radiative transitions. In those cases where the electron densities and temperatures were derived from lines of the same ionic species, this has been done in a self-consistent, iterative manner. The slow variation of the effective collision strengths with temperature has been included in the model.

Table 2. The ionic fractions as derived from the optical and infrared line fluxes. For N11A, the two differently derived infrared ionic fractions are given (see Sect. 3.2). No infrared ionic fractions could be derived for N79A. The notation $a(-b)$ is shorthand for $a \times 10^{-b}$.

Object	$(O^+/H^+)_{Op}$	$(O^{++}/H^+)_{Op}$	$(N^+/H^+)_{Op}$	$(S^+/H^+)_{Op}$	$(S^{++}/H^+)_{Op}$	$(S^{++}/H^+)_{Ir}$	$(S^{+3}/H^+)_{Ir}$
N81	1.84 (−5)	7.33 (−5)	5.26 (−7)	1.49 (−7)	1.20 (−6)	8.31 (−7)	2.13 (−7)
N88A	1.24 (−5)	6.56 (−5)	3.91 (−7)	3.57 (−8)	1.06 (−6)	3.53 (−7)	4.75 (−7)
N66	2.20 (−5)	8.32 (−5)	7.59 (−7)	2.45 (−7)	1.53 (−6)	1.30 (−6)	4.19 (−7)
N79A	6.34 (−5)	8.28 (−5)	3.43 (−6)	5.13 (−7)	6.38 (−6)	–	–
N4A	6.09 (−5)	1.36 (−4)	2.50 (−6)	3.53 (−7)	4.55 (−6)	4.32 (−6)	6.54 (−7)
N83B	4.87 (−5)	1.14 (−4)	3.25 (−6)	5.22 (−7)	4.36 (−6)	2.25 (−6)	2.40 (−7)
N11A[1]	6.82 (−5)	1.41 (−4)	3.54 (−6)	5.15 (−7)	4.03 (−6)	2.47 (−6)	2.88 (−7)
N11A[2]						4.33 (−6)	6.80 (−7)
N159-5	6.65 (−5)	7.37 (−5)	3.23 (−6)	6.91 (−7)	7.00 (−6)	6.81 (−6)	8.03 (−7)
N157B	1.08 (−4)	4.31 (−5)	4.77 (−6)	1.18 (−6)	5.17 (−6)	4.29 (−6)	2.35 (−7)
30 Dor#1	3.71 (−5)[3]	1.39 (−4)	8.93 (−7)	1.28 (−7)	3.52 (−6)	7.56 (−6)	1.32 (−6)
30 Dor#2	5.06 (−5)[3]	1.37 (−4)	7.73 (−7)	1.61 (−7)	3.19 (−6)	6.15 (−6)	1.46 (−6)
30 Dor#3	3.93 (−5)[3]	1.40 (−4)	1.53 (−6)	1.67 (−7)	4.36 (−6)	5.54 (−6)	1.48 (−6)
30 Dor#4	7.01 (−5)[3]	1.15 (−4)	2.00 (−6)	2.85 (−7)	3.36 (−6)	8.73 (−6)	1.27 (−6)
N160A1	6.96 (−5)	1.45 (−4)	3.28 (−6)	5.07 (−7)	5.68 (−6)	6.57 (−6)	1.15 (−6)
N160A2	7.94 (−5)	1.45 (−4)	3.61 (−6)	5.34 (−7)	5.67 (−6)	4.84 (−6)	6.70 (−7)

Object	$(Ar^+/H^+)_{Ir}$	$(Ar^{++}/H^+)_{Op}$	$(Ar^{++}/H^+)_{Ir}$	$(Ne^+/H^+)_{Ir}$	$(Ne^{++}/H^+)_{Op}$	$(Ne^{++}/H^+)_{Ir}$	$(He^+/H^+)_{Op}$
N81	–	3.95 (−7)	2.35 (−7)	2.47 (−6)	1.51 (−5)	7.86 (−6)	0.082
N88A	–	3.74 (−7)	3.15 (−7)	–	1.33 (−5)	5.60 (−6)	0.089
N66	–	3.81 (−7)	6.57 (−7)	1.27 (−5)	1.57 (−5)	1.74 (−5)	0.084
N79A	–	1.25 (−6)	–	–	1.39 (−5)	–	0.084
N4A	–	1.11 (−6)	1.13 (−6)	2.28 (−5)	2.69 (−5)	2.87 (−5)	0.088
N83B	–	1.09 (−6)	8.05 (−7)	1.58 (−5)	1.65 (−5)	9.60 (−6)	0.084
N11A[1]	–	1.18 (−6)	7.07 (−7)	1.63 (−5)	3.48 (−5)	1.60 (−5)	0.089
N11A[2]			1.67 (−6)	2.86 (−5)		2.80 (−5)	
N159-5	–	1.39 (−6)	1.68 (−6)	4.63 (−5)	1.83 (−5)	5.97 (−5)	0.093
N157B	–	1.04 (−6)	1.13 (−6)	3.50 (−5)	6.69 (−6)	2.66 (−5)	0.097
30 Dor#1	–	9.37 (−7)	1.34 (−6)	2.33 (−5)	–	5.34 (−5)	0.087
30 Dor#2	–	8.85 (−7)	1.14 (−6)	2.02 (−5)	3.63 (−5)	6.04 (−5)	0.091
30 Dor#3	–	1.16 (−6)	1.45 (−6)	2.03 (−5)	3.79 (−5)	5.84 (−5)	0.094
30 Dor#4	–	8.46 (−7)	1.50 (−6)	3.02 (−5)	3.88 (−5)	7.37 (−5)	0.086
N160A1	1.04 (−7)	1.34 (−6)	1.42 (−6)	2.82 (−5)	3.00 (−5)	4.72 (−5)	0.087
N160A2	1.58 (−7)	1.37 (−6)	1.33 (−6)	2.68 (−5)	3.04 (−5)	3.07 (−5)	0.084

[1] Infrared ionic fractions calculated with the Brβ flux as derived from the Hβ line (see Sect. 3.2).

[2] Ionic fractions calculated from infrared line fluxes scaled to the Brβ aperture (see Sect. 3.2).

[3] Derived from the $(S^{++}/S^+) - (O^{++}/O^+)$ relation from Vermeij & van der Hulst, in preparation.

The effective collision strengths and radiative transition probabilities have been taken from many different sources, but mainly from the IRON project. Effective collision strengths have been taken from Saraph & Tully (1994, Ne^+), Butler & Zeippen (1994, Ne^{++}), Pelan & Berrington (1995, Ar^+), Galavis et al. (1995, Ar^{++}, S^{++}), Cai & Pradhan (1993, S^+), Saraph & Storey (1999, S^{+3}), Lennon & Burke (1994, N^+, O^{++}) and McLaughlin & Bell (1998, O^+). The radiative transition probabilities have been taken from Cai & Pradhan (1993, S^+), Biemont & Bromage (1983, S^{++}), Galavis et al. (1997, N^+, O^{++}, Ne^{++}), Mendoza & Zeippen (1983, Ar^{++}) and Mendoza (1983, Ne^+, Ar^+, S^{+3}). The O^+ transition probabilities have been taken from the CHIANTI database.

3.1. Properties of the electron gas

The electron temperatures were determined from optical line ratios only, and were derived for the O^+, O^{++} and S^{++} emitting zones. For this we used the [O III] (5007 + 4959)/4363, the [S III] 9068/6312 and the [O II] (3727+3730)/(7320+7330) line ratios. Where more than one scan spectrum was available for an object, we determined the temperature from the average of the line ratios from the different spectra. The [N II] 5755 Å and [S II] 4068, 4076 Å lines were not detected or were too weak to derive a T_e [N II] or T_e [S II] from. No attempt was made to derive electron temperatures from line ratios combining the optical and the infrared lines. The different ways in which

the optical and various infrared lines were observed would make such ratios very hard to interpret.

The driftscan spectra for the sources N83B, N11A and the pointings in 30 Doradus did not include the [O II] (3727 + 3730) Å or [Ne III] 3869 Å lines so no T_e [O II] could be derived from them. We therefore used our stationary longslit spectra centered on N83B and N11A to cure that problem. In order to obtain a T_e [O II] for the 30 Dor positions, we used the results from an extensive spectroscopic study of 30 Doradus with spectral positions covering the face of the nebula (Vermeij & van der Hulst, in prep.). This was unfortunately not possible for the pointing 30 Dor#1.

The electron density in the S^+ zone was derived from the classical optical ratio of [S II] 6717/6730. The ratio was not taken from the scan spectra but from longslit spectra centered on the same position as the scan spectra. This was necessary because in the scan spectra the line ratio is always in the low-density regime where it loses its sensitivity to the electron density. In the few cases where this was not possible, an electron density of 500 cm^{-3} was adopted.

The electron densities in the S^{++} and O^{++} zones were derived from the infrared lines. The O^{++} density was derived from the [O III] 52 μm/88 μm and the S^{++} density from the [S III] 18 μm/33 μm ratio. In almost all cases, the [O III] 52 μm/88 μm line ratio was in the low-density regime. For the [S III] 18 μm/33 μm ratio, an aperture correction had to be applied, because all the ratios, except for N88A, were unphysically low. The derived electron densities and temperatures are given in Table 1.

3.2. Ionic fractions

The ionic fractions were calculated from the forbidden lines with the usual equation

$$\frac{X^+}{H^+} = \left[\frac{I_\lambda}{I_{H^+}}\right]\left[\frac{\epsilon(n_e, T_e)}{A_\lambda E_\lambda}\right]\left[\frac{n_e}{F(n_e, T_e)}\right], \quad (1)$$

with X^+/H^+ the ionic fraction, I_λ/I_{H^+} the line flux relative to the hydrogen recombination line Brβ or Hβ, A_λ and E_λ the radiative rate and energy of the transition from which the line originates, $\epsilon(n_e, T_e)$ the emissivity of the hydrogen recombination line taken from Storey & Hummer (1995), n_e and T_e the electron density and temperature, and $F(n_e, T_e)$ the level-distribution function.

For some ionic species the fraction could be calculated from the infrared as well as from the optical line flux. This is the case for species of which the infrared lines have a suitable hydrogen recombination line available. The S^{++}, Ar^{++} and Ne^{++} ionic fractions could be calculated this way. The hydrogen recombination line used in all cases was the Brβ line. To get the best possible aperture match with the Brβ flux, the [Ne III] 15.6 μm and [S III] 18.7 μm lines were used instead of the [Ne III] 36.0 μm and [S III] 33.4 μm lines. The absence of a suitable hydrogen recombination line in the LWS spectral range made it impossible to derive an O^{++} ionic fraction from the [O III] 52 μm and [O III] 88 μm lines. For the remainder of this paper, the differently derived ionic fractions will be referred to as the optical and infrared ionic fractions, respectively.

No Brβ flux was available for N11A so we had to derive it from the Hβ line in the optical driftscan spectra. This procedure, however, introduced a severe "aperture" mismatch between the derived Brβ flux and the infrared line fluxes. The flux in the 1D driftscan spectrum of N11A is the sum from an area of the sky covering 24″ × 36″ whereas the infrared line fluxes are observed through apertures of 14″ × 20″ and 14″ × 27″. We therefore calculated the infrared ionic fractions for N11A in two different ways. A lower limit of the ionic fraction was derived by just using the derived Brβ flux. A second value for the ionic fraction was derived by scaling the infrared line fluxes to the Brβ aperture. Both ionic fractions are given in Table 2.

Because of the smaller spectral coverage of the scan spectra of N11A, N83B and 30 Doradus, the O^+_{opt} and Ne^{++}_{opt} ionic fractions had to be derived from their stationary longslit spectra and from the spectra of the more extensive study of 30 Doradus already mentioned in Sect. 3.1. The O^+_{opt} fraction for the pointings in 30 Dor was determined from the relation between the (S^{++}/S^+) and (O^{++}/O^+) ratios derived in the study of this object using the $(S^{++}/S^+)_{opt}$ ratio and O^{++}_{opt} ionic fraction from the present work. We used the [Ne III] 3869 Å line from these spectra to derive the Ne^{++}_{opt} fraction for our positions in 30 Doradus.

For the calculation of the He^+ ionic fraction the following equation was used

$$\frac{He^+}{H^+} = \left[\frac{I_\lambda}{I_{H\beta}}\right]\left[\frac{\epsilon_\beta(n_e, T_e)}{\epsilon_\lambda(n_e, T_e)}\right], \quad (2)$$

with $I_\lambda/I_{H\beta}$ the helium line flux relative to the Hβ line, $\epsilon_\beta(n_e, T_e)$ the Hβ emissivity from Storey & Hummer (1995), and $\epsilon_\lambda(n_e, T_e)$ the helium recombination line emissivity from Benjamin et al. (1999). The He I recombination lines used in the derivation were the λ 5875 Å and the λ 6680 Å lines. The He^+ fraction derived from the two different lines was then averaged to produce the final result.

Where possible, the ionic fractions have been calculated using the electron density and temperature appropriate for the zone in which the particular ion resides. The T_e [O II] is, however, so sensitive for the electron density used that this one has not been used for this purpose. The S^{++} and Ar^{++} ionic fractions have been calculated with T_e [S III], while for the other ions T_e [O III] has been used. The ionic fracions are given in Table 2.

4. Discussion

4.1. Electron temperatures

The various electron temperatures derived for our sources are given in Table 1. All these temperatures have values near or higher than 10 000 Kelvin. The SMC sources are a bit hotter than the LMC ones, but this is a known effect of their different metallicities. The T_e [O III] are generally a bit higher than found in the literature for our sources, which is the result of different line ratios and more recent atomic data. The T_e [S III] are comparable to the [O III] temperatures, but the uncertainties are somewhat larger. This is due to the lines used in their derivation; the [S III] 6312 Å line is quite weak (typically ∼1.5% of Hβ) and the uncertainty on the [S III] 9068 Å

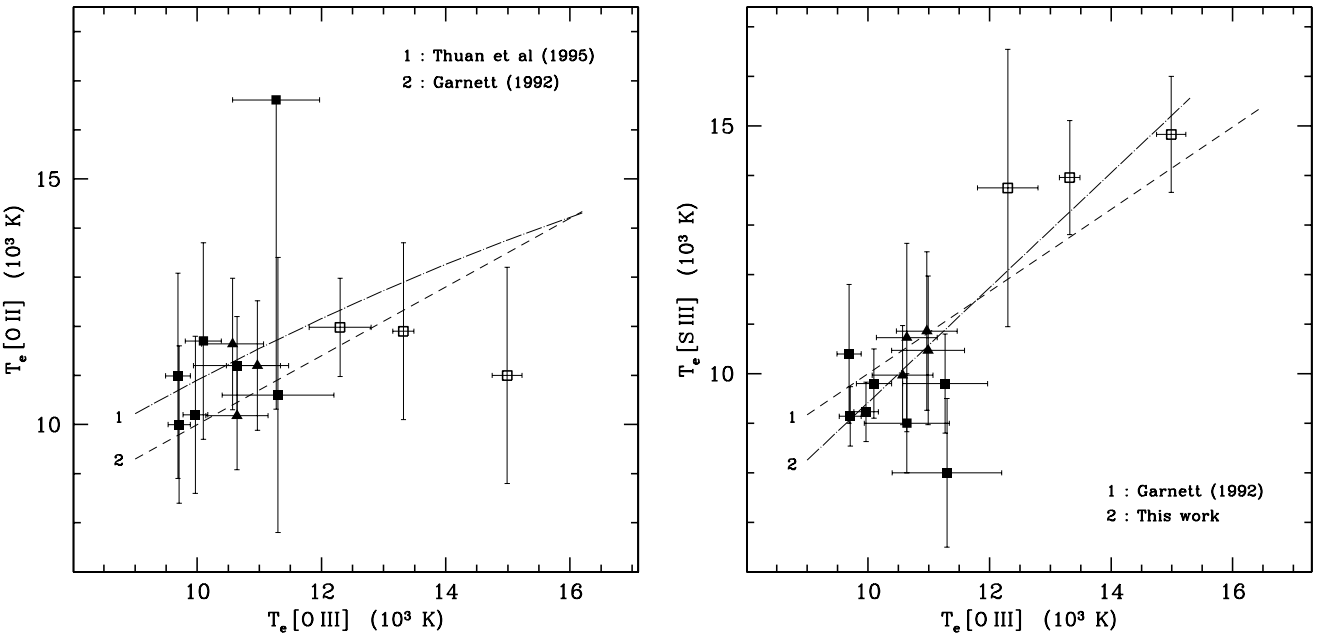

Fig. 1. The correlation between T_e [O III] and T_e [O II] (*left*) and T_e [S III]. The SMC sources are given as open squares, the 30 Doradus pointings as solid triangles and the other LMC sources as solid squares.

is increased due to an unknown amount of telluric absorption. The T_e [O II] have uncertainties between 10 and 20%. This results from the fact that for a given [O II] (3727 + 3730)/(7320 + 7330) ratio the derived temperature is very sensitive to the electron density; an uncertainty in the electron density of 100 cm^{-3} translates into an uncertainty in T_e [O II] of as much as 500 Kelvin.

It is important to point out that the electron temperatures have been derived from optical *drift*scan spectra. Any small temperature fluctuation across the area covered by the spectra weighs the flux of the temperature-sensitive lines towards regions where the temperature is slightly higher, which can increase the temperatures found in this analysis.

4.1.1. Temperature stratification

The electron temperature is a crucial ingredient in the derivation of elemental abundances, and the high sensitivity of the abundances to the temperatures makes a good determination of these very important. Large-scale temperature gradients and small-scale temperature fluctuations have a large impact on the abundances one derives.

The once widely adopted assumption in abundance studies of an isothermal H II region has been replaced by a more sophisticated two-zone treatment of the large-scale temperature stratification. In this treatment, a subdivision has been made in a T_e [O II] zone for N^+ and O^+ and a T_e [O III] zone for Ne^{++}, O^{++}, Ar^{++} and S^{++}. A further refinement to this scheme was later introduced by Garnett (1992), treating Ar^{++} and S^{++} in their own, separate third temperature zone.

Given the importance of the electron temperature for the correct derivation of the abundances, attempts have been made to find relations between the different temperatures. Garnett (1992) derives the following relations between these from fits to photoionization models covering a large range of metallicities

$$t_e\,[\mathrm{O\,II}] = 0.70\,t_e\,[\mathrm{O\,III}] + 0.30 \quad (3)$$

$$t_e\,[\mathrm{S\,III}] = 0.83\,t_e\,[\mathrm{O\,III}] + 0.17 \quad (4)$$

with t_e in units of 10^4 K. An alternative relation for t_e [O II] derived by Thuan et al. (1995) is

$$t_e\,[\mathrm{O\,II}] = 0.243 + t_e\,[\mathrm{O\,III}]\,(1.031 - 0.184\,t_e\,[\mathrm{O\,III}]). \quad (5)$$

These relations are shown in Fig. 1 together with our measured temperatures.

The derived electron temperatures for the O^{++} and O^+ zone generally fall right in between the relations given by Eqs. (3) and (5) (Fig. 1, left panel), with the latter relation predicting a higher T_e [O II] than the former for temperatures up to about 16 000 K. The grossly deviating point is that of N83B. The N88A temperature-pair is lower than the relations predict but is still within 1.5 σ from them. The T_e[O II] for N88A, however, might have been depressed a bit because of the very high n_e[S II] found for this object.

The same general agreement with the predictions is seen in the righthand panel of Fig. 1 for T_e [S III] as a function of T_e [O III]. The temperatures agree reasonably well with Eq. (4), especially near 10 500 K. However, despite the fact that the derived temperature-pairs are consistent within their errors with the theoretical relation from Garnett (1992), most of the low-end points fall below this relation whereas the SMC high-end points all lie above it. We therefore derived a new linear empirical relation between T_e [S III] and T_e [O III]. To this end, a least-squares fit has been made to the data points taking into account the errors in both the temperatures. The procedure followed is the one given by Reed (1989). The derived fit is plotted in Fig. 1. The fit parameters for the slope and the intercept are

1.16 ± 0.12 and -0.22 ± 0.13, respectivly, in units of 10^4 K. The inclusion of the point for N159-5 with its low T_e [S III] did not change these parameters much. The large uncertainty on the derived intercept is mainly the result of the often substantial errors on T_e [S III].

The fact that our sample objects are located in the Magellanic Clouds limits our discussion of the temperature relations to the low-metallicity end of these, but we can conclude that at least in this regime the different relations between the electron temperatures derived from photoionization models are quite accurate. The relation between T_e [S III] and T_e [O III], however, could be a bit steeper than predicted.

We did not address the subject of small-scale temperature fluctuations, although the optical and infrared fine-structure lines in our database combined, in principle, make it possible to determine their presence and, if there are any, to measure their size. However, the multitude of different instruments, beams and apertures used in obtaining our optical and infrared fluxes makes the interpretation of the optical/infrared ratios necessary for this analysis extremely difficult. We therefore could not carry out this analysis here.

4.2. Electron densities

The electron densities presented in Table 1 are all lower than 1000 cm^{-3} except for the object N88A. The O^{++} electron densities were derived from lines observed through the large LWS beam, which samples the more diffuse part of many of our objects. All the O^{++} densities are therefore quite low. The infrared lines used in the determination of n_e[S III] were observed through two different ISO-SWS apertures. In nearly all cases, this resulted in a [S III] 18.7 μm/[S III] 33.4 μm ratio that was unphysically low, i.e. the line ratio was lower than possible given the atomic physics of the S^{++} ion. We therefore scaled the [S III] 18.7 μm line flux with a factor equal to the ratio of the areas covered by the two apertures. The electron densities derived for N88A are all in the order of ~2000 cm^{-3}, this despite the ambiguities in the [O III] and [S III] line ratios. The [Ne III] 15.6 μm/[Ne III] 36.0 μm density diagnostic could not be used for our objects because of the high critical density (10^{4-5} cm^{-3}) of the ratio.

4.3. Full elemental abundances and ICFs

4.3.1. Error budget of the ionic fractions

The factors that contribute to the uncertainty in the derived ionic fractions include errors in the used temperature and density, uncertainties in the fluxes, and uncertainties in the used atomic data. This last source of error is rather intractable, however, and shall not be discussed here.

The contribution of the flux uncertainties to the total error budget is relatively low for the optical lines. With errors of typically 5% for the strong optical line fluxes, the optical ionic fractions are hardly affected by it. The exception in this case is the [S III] 9068 Å flux from which the S^{++}_{opt} ionic fraction is calculated. This line suffers from telluric absorption that can increase the uncertainty on the flux with ~20% (see Paper I). As far as the infrared line fluxes are concerned, the instrumental setup of the ISO spectrometers imposes its own typical set of uncertainties on the lines (see Paper I for a discussion), but if one confines oneself to the combined uncertainty in the flux calibration and flux measurement, the uncertainties in the used infrared fluxes are commonly around 10%.

The uncertainties in the applied electron temperature and density both have their own different impact on the ionic fractions. Furthermore, not every ion reacts the same to changes in these parameters. Although it is very difficult to propagate the error in the ionic fractions through Eq. (1) in a formal manner, an estimate of the resulting error can be obtained by varying the temperature and density within their error bars.

The size of the contribution to the total error in the ionic fractions due to uncertainties in the electron density depends on the fine-structure level configuration of the relevant ion; five-level ions with a low-lying triplet like O^{++} are much less sensitive to the density than those with a low-lying singlet (O^+ and S^+). It turns out that for the generally low densities observed in our sample objects, an uncertainty of 200 cm^{-3} in the density will translate into less than 1% error in the ionic fraction of O^{++}_{opt}, Ne^{+}_{ir}, Ne^{++}_{opt}, Ne^{++}_{ir}, S^{++}_{opt}, Ar^{+}_{ir}, Ar^{++}_{opt}, Ar^{++}_{ir} and N^{+}_{opt}. For O^{+}_{opt} and S^{+}_{opt} though this error increases to 4% and 10% respectively, while both the S^{++}_{ir} and S^{+3}_{ir} fractions have their errors increased by about 4%.

The largest contribution to the total error is produced by the uncertainty in the electron temperature. A variation of 900 K in temperature can produce an error of ~20% for O^{+}_{opt}, O^{++}_{opt} and Ne^{++}_{opt}, and ~10% for S^{+}_{opt} and S^{++}_{opt}. The error is ~15% for Ar^{++}_{opt} and N^{++}_{opt}. The ionic fractions derived from the infrared lines suffer much less from errors in the electron temperature. The impact of the uncertainty in the electron temperature here is about 5% for all the infrared ionic fractions.

Taking into account both of the sources of error discussed here, we derived a typical error of 15% for the optical ionic fractions and of 10% for the infrared ones. For some specific cases like S^{++}_{opt} this error increases to ~25%. The estimates are probably somewhat conservative because both the electron properties and ionic fractions are ultimately derived from the same set of line fluxes so some cancellation is possible. A quick glance at Eq. (1) suffices to see that the errors are not independent.

The error analysis given above only applies to the ionic fractions derived from fine-structure lines. The uncertainty in the He^+ ionic fraction, which is derived from recombination lines, arises from the impact of the uncertainty of the electron temperature on the helium line-emissivities. This impact is, however, small. A variation of 900 K in temperature translates itself into an uncertainty of ~3% in the ionic fraction. The uncertainty on the helium line fluxes is larger (between 5 and 10%).

4.3.2. Comparison between the optical and infrared ionic fractions

An extra check on the reliability of the S^{++}, Ar^{++} and Ne^{++} ionic fractions was performed by comparing the optical

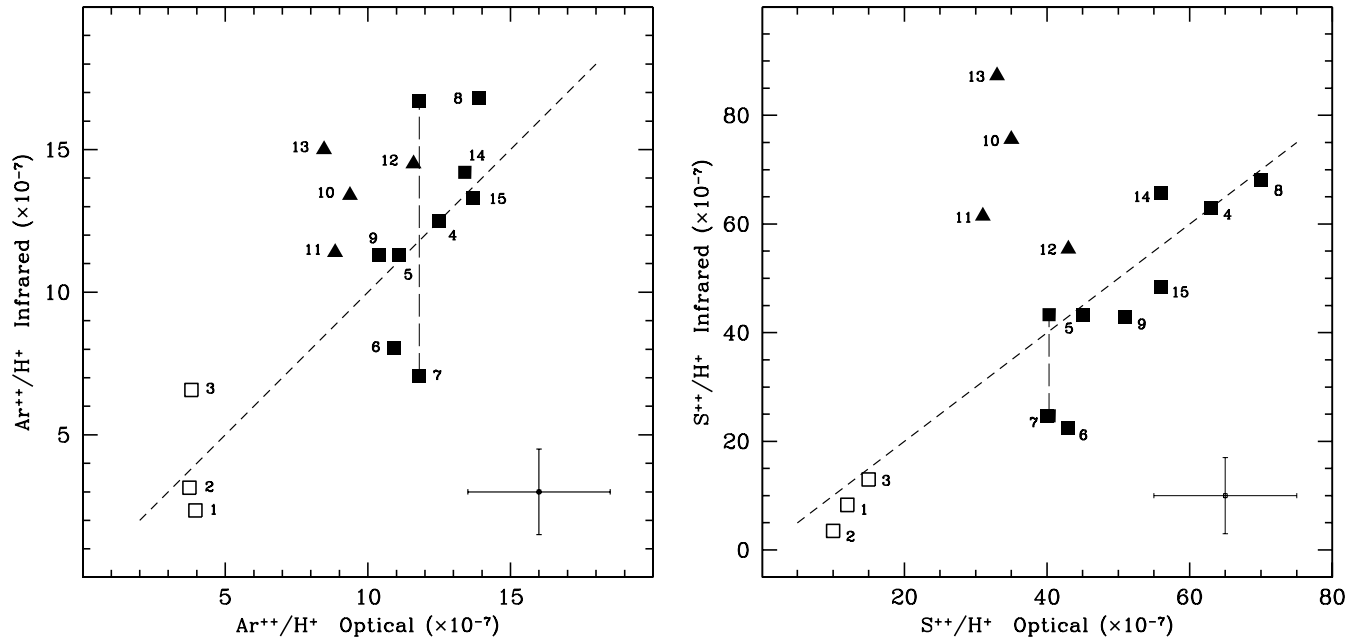

Fig. 2. The comparison between the S^{++} and Ar^{++} ionic fractions as derived from the optical and infrared fluxes. The SMC sources are given as open squares, the 30 Doradus pointings as solid triangles and the other LMC sources as solid squares. The numbering of the objects is according to Table 1. The vertical dashed line connects the two differently derived infrared ionic fractions of N11A (see Sect. 3.2). Shown in the right lower corner is a typical error bar.

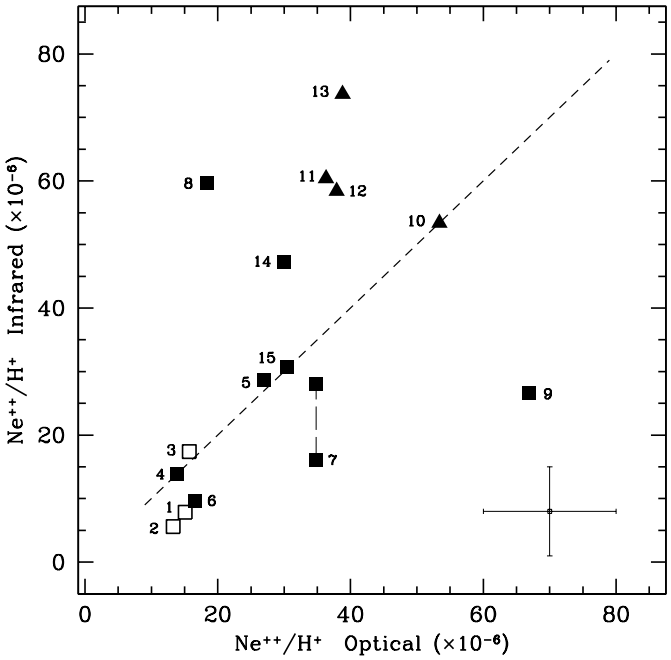

Fig. 3. The comparison between the Ne^{++} ionic fractions as derived from the optical and infrared fluxes. For an explanation of the symbols and labels see Fig. 2. The vertical dashed line connects the two differently derived infrared ionic fractions of N11A (see Sect. 3.2). Shown in the right lower corner is a typical error bar.

fractions with the infrared ones. As Figs. 2 and 3 show, there is in general a reasonable agreement between the different S^{++} and Ar^{++} ionic fractions. The Ne^{++} ionic fraction is the least certain of the three showing a large scatter. The largest differences are found for the more extended objects.

The use of T_e [S III] rather than T_e [O III] in the derivation of the S^{++} and Ar^{++} ionic fractions cannot explain the differences. For many of our sample objects, and especially for our pointings in 30 Doradus, the T_e [S III] and T_e [O III] are rather similar. Also, in order to get equal optical and infrared ionic fractions for e.g. the pointings in 30 Doradus one has to lower the T_e [S III] which would in turn make the relation between T_e [S III] and T_e [O III] derived in Sect. 4.1.1 even steeper.

The most likely explanation for the differences between the optical and infrared ionic fractions is the difference in the area of the sky covered by the optical driftscan spectra and the ISO-SWS beams. The optical driftscan spectra usually cover a somewhat larger area than the SWS apertures through which the infrared line fluxes have been observed. Our sample objects are all spatially resolved and variations in the ionization structure across the beam can play an important role. This problem is the most severe for large extended objects such as 30 Doradus (positions 10–13 in Figs. 2 and 3).

4.3.3. Ionization correction factors

The most difficult step in the derivation of elemental abundances is the correction one has to make for the unobserved ionic species of an element. The factors used in this correction are commonly called Ionization Correction Factors (ICFs).

An early prescription for ICFs was given by Peimbert & Costero (1969). Based on coincidences of ionization potentials a scheme for the ICFs was developed in which the H II region was divided into two parts. The boundary between these two parts is defined by the ionization potential of O^+ (35.1 eV) and S^{++} (34.8 eV). In this scheme, the low-ionization (N^+, S^+, O^+, Ne^+) and high-ionization species (like O^{++} and Ne^{++}) reside in

their own separate parts of the nebula. The ICF for a particular element was then taken to be O/O^{+} or O/O^{++} for the low and high-ionization species, respectively.

The simple two-zone model for the ICFs, however, soon broke down. The inclusion of more atomic properties than only the ionization potential (e.g. Natta et al. 1980) and of more processes playing a role in determining the ionization structure (e.g. charge-transfer reactions) showed the scheme to be oversimplified. This is best seen in the case of sulfur and also argon, for which more elaborate prescriptions for the ICFs had to be constructed.

As a legacy of these early attempts, ionization correction factors are usually given as a function of the fraction O^{+}/O or O^{++}/O combined with the assumption that $O = O^{+} + O^{++}$. The neon and nitrogen abundances are then calculated from the relation

$$\frac{Ne}{Ne^{++}} = \frac{O}{O^{++}} \tag{6}$$

and with

$$\frac{N}{N^{+}} = \frac{O}{O^{+}}, \tag{7}$$

where the ICFs are simply the inverted O^{++}/O and O^{+}/O fractions.

The correction factors for sulfur and argon are usually derived from fits to photoionization models. Fits to models from Stasińska (1978) give for the sulfur ICFs the relation

$$\frac{S}{S^{+} + S^{++}} = \left[1 - \left(1 - \frac{O^{+}}{O}\right)^{\alpha}\right]^{-1/\alpha} \tag{8}$$

with $2 < \alpha < 3$. This ionization correction factor is also employed for argon (e.g. Oey & Shields 2000). More elaborate descriptions for sulfur and argon given by Thuan et al. (1995) are

$$\frac{S}{S^{+} + S^{++}} = [\,0.013 + x(5.10 - x(12.78 - x(14.77 - 6.11x)))\,]^{-1} \tag{9}$$

$$\frac{Ar}{Ar^{++}} = [\,0.15 + x(2.39 - 2.64x)\,]^{-1} \tag{10}$$

with $x \equiv O^{+}/O$. With our data base including fine-structure lines from species like Ne^{+} and S^{+3} it is possible to check the ICFs for neon and sulfur as given in these equations.

The sulfur ICFs as defined in Eqs. (8) and (9) have been compared with the observed ratio $(S^{+} + S^{++} + S^{+3})/(S^{+} + S^{++})$. The results are shown in the left panel of Fig. 4. Also shown in this figure is a more recent prescription for the sulfur ICF from Kwitter & Henry (2001). The error bars in this figure give the range of the plotted ratio when using either the optical or infrared S^{++} ionic fraction in the sum.

As can be seen in this figure, the observed sum abundances compare reasonably well with the total abundances predicted by the theoretical ICFs. Many of the observed sulfur abundances agree well with the ICF from Eq. (8) using $\alpha = 3$, and with the ICF from Kwitter & Henry (2001). The prescription for the ICF from Thuan et al. (1995) clearly overpredicts the amount of "missing" sulfur. The value for α to adopt in Eq. (8) is not completely clear. In the original prescription by Stasińska (1978) the value of 3 was used, but French (1981) took α to be 2. Garnett (1989) pointed out, however, that the use of $\alpha = 2$ severely overpredicts the amount of unobserved sulfur for O^{+}/O in the range from 0.1 to 0.3. This is clearly seen in Fig. 4 where the $\alpha = 2$ ICF is even larger than the one from Thuan et al. (1995). It was also noted by Garnett (1989) that although the use of $\alpha = 3$ gives a good correction for the unobserved sulfur, it seemed to underestimate the missing sulfur for $O^{+}/O < 0.2$. The ICF from Kwitter & Henry (2001) is even lower in this range.

Given our observational results, we conclude that the prescription for the sulfur ICF given in Eq. (8) with $\alpha = 3$ is fairly accurate for $O^{+}/O > 0.2$. For $O^{+}/O < 0.2$ the case is less clear, but one might argue that the ICF as a function of O^{+}/O is steeper in this range. It is, however, difficult to check this last statement in this work because our only point with $O^{+}/O < 0.2$ shows a large variation in the $(S^{+} + S^{++} + S^{+3})/(S^{+} + S^{++})$ ratio. The number of ionization stages included in the $\sum S^{+i}/(S^{+} + S^{++})$ ratio has of course some influence on our results, but with the ionization potential of S^{+3} as high as it is (47.3 eV), we do not think that the inclusion of ionization stages higher than this will change our conclusions.

Shown in the right panel of Fig. 4 is the comparison between the $(Ne^{+} + Ne^{++})/Ne^{++}$ ratio and the ICF from Eq. (6). For the error bars in this figure the same remarks apply as for sulfur. The large scatter and uncertainty in the Ne^{++} ionic fraction already noted (cf. Sect. 4.3.2) make the situation rather unclear. At first sight the theoretical ICF for neon seems to underestimate the true neon abundances. The observed Ne/Ne^{++} ratio, however, strongly depends on the ionization structure one happens to find in the beam (i.e. the ratio Ne^{+}/Ne^{++}). If for whatever reason the Ne^{+}/Ne^{++} ratio is increased, the observed Ne/Ne^{++} ratio can quite easily exceed the value predicted by the theoretical ICF. This problem, of course, also plays a role for sulfur, but in this case the S^{+3} ionic fraction is compared to the sum of *two* other ionization stages (of which S^{++} is the dominant one) so the impact is less. Given this confused state of affairs, we feel that we cannot draw any strong conclusion about the (un)reliability of the neon ICF given in Eq. (6).

The Ar^{+} ionic fraction could unfortunately only be calculated for two of our sample objects, so a comparison of the argon abundance with the theoretical ICFs is difficult. The observed ratio $(Ar^{+} + Ar^{++})/Ar^{++}$ for N160A1 and N160A2 are 1.08 and 1.12, respectively. The argon ICFs for N160A1 and N160A2 are 1.54 and 1.51 using the prescription in Eq. (10). Using Eq. (8), the ICFs are 1.20 and 1.18 for $\alpha = 2.5$, and 1.18 and 1.11 for $\alpha = 3.0$. The latter ICFs are quite close to the $(Ar^{+} + Ar^{++})/Ar^{++}$ ratios found for N160A1 and N160A2, but whether this means that this particular ICF is "correct" is not clear; the presence of Ar^{+3} would raise the $\sum Ar^{+i}/Ar^{++}$ ratio. The ionization potential of Ar^{++} is about the same as that of Ne^{+} (~40 eV), so it is conceivable that some Ar^{+3} is present in the source.

The only source for which the presence of Ar^{+3} was detected is 30 Doradus#3 where it showed up in the form of the

Table 3. The full elemental abundances of O, N, S, Ar, Ne and He. A comparison is made with abundances from the literature. The first row for every entry gives the abundances from the present work. The use of ICFs has been limited to the derivation of the full N and Ar abundances. For N79A, however, ICFs have also been used for the derivation of the full elemental abundances of S and Ne (see text).

		N81	N88A	N66	N4A	N83B	N159-5	N157B	N79A
O/H	(10^{-4})	0.917 0.791[1] 0.994[4]	0.780 1.11[2] 0.781[4]	1.05 1.66[3] 1.12[4]	1.97 2.66[5] 2.77[4]	1.63 1.94[6]	1.40 2.33[7] 2.09[4] (N159A)	1.51	1.46 2.54[4]
N/H	(10^{-6})	2.63 2.16[1] 3.14[4]	2.44 2.20[4]	3.61 3.16[3] 4.17[4]	8.07 11.3[5] 9.83[4]	10.8 7.00[6]	6.87 7.68[7] 6.98[4] (N159A)	4.77‡	7.91 10.6[4]
S/H	(10^{-6})	1.38 ± 0.18 1.12[1]	1.22 ± 0.35 3.47[2]	2.08 ± 0.12 6.61[3]	5.45 ± 0.12 5.99[5] 17.9[4]	4.07 ± 1.05 4.40[6]	8.40 ± 0.10 3.78[7] ± 0.84	6.15 ± 0.44	7.37
Ar/H	(10^{-6})	0.400 ± 0.102 0.758[1] 0.808[4]	0.465 ± 0.040	0.650 ± 0.173 0.812[3]	1.29 ± 0.01 1.53[5]	1.09 ± 0.16	1.62 ± 0.15	1.09‡ ± 0.05	1.34
Ne/H	(10^{-5})	1.40 ± 0.36 1.49[1] 1.73[4]	0.945† ± 0.039 2.19[2] 1.42[4]	2.93 ± 0.09 3.02[3] 1.95[4]	5.06 ± 0.09 3.21[5] 5.28[4]	2.89 ± 0.35 4.00[6]	8.53 ± 2.07 1.90[7] 3.98[4] (N159A)	5.17 ± 1.00	2.45 3.63[4]
He/H		0.082 0.088[1]	0.089 0.078[2]	0.084 0.072[3]	0.088 0.08[5]	0.084 0.10[6]	0.093 0.092[7]	0.097	0.084
		N160A1	N160A2	30 Dor#1	30 Dor#2	30 Dor#3	30 Dor#4	N11A (1)	N11A (2)
O/H	(10^{-4})	2.15 2.76[7] 2.78[4] (N160A)	2.24 2.16[7]	1.76 2.12[8] 2.03[9] 2.57[3]	1.88	1.79	1.85	2.09 2.79[7]	
N/H	(10^{-6})	9.94 8.08[7] 8.13[4] (N160A)	10.3 6.57[7]	4.25 7.63[8] 5.71[9] ± 0.38 6.17[3]	2.86	6.96	5.26	10.7 7.31[7]	
S/H	(10^{-6})	7.79 ± 0.45 6.75[7] ± 1.92 18.2[4] (N160A)	6.46 ± 0.42 4.88[7] ± 1.32	6.99 ± 2.02 5.09[8] 4.63[9] ± 0.09 7.94[3]	6.29 ± 1.48	6.60 ± 0.59	7.61 ± 2.69	4.05 ± 0.78 3.89[7] ± 1.06	5.38 ± 0.15
Ar/H	(10^{-6})	1.48⋆ ± 0.04 1.26[4] (N160A)	1.51⋆ ± 0.02	1.43 ± 0.25 1.06[8] 1.79[9] ± 0.17 1.38[3]	1.19 ± 0.15	1.62 ± 0.18	1.28 ± 0.36	1.07 ± 0.26	1.61 ± 0.28
Ne/H	(10^{-5})	6.68 ± 0.86 6.33[7] 5.01[4] (N160A)	5.73 ± 0.02 4.48[7]	7.67 3.58[8] 6.08[9] ± 0.88 5.13[3]	6.86 ± 1.21	6.85 ± 1.03	8.65 ± 1.75	4.17 ± 0.94 5.06[7]	6.00 ± 0.34
He/H		0.087 0.087[7] ± 0.002	0.084 0.081[7] ± 0.003	0.087 0.081[9]	0.091	0.094	0.086	0.089 0.085[7]	

† Only the Ne^{++} abundance is given. No Ne^{+} abundance was available for this object.
‡ No ICF was used. ⋆ The sum abundance Ar^{+} + Ar^{++} is given. No ICF was used.
[1] Heydari-Malayeri et al. (1988), [2] Testor & Pakull (1985), [3] Shaver et al. (1983), [4] Pagel et al. (1978),
[5] Heydari-Malayeri & Lecavalier des Etangs (1994), [6] Heydari-Malayeri, van Drom & Leisy (1990),
[7] Heydari-Malayeri & Testor (1986), [8] Rosa & Mathis (1987), [9] Mathis et al. (1985).

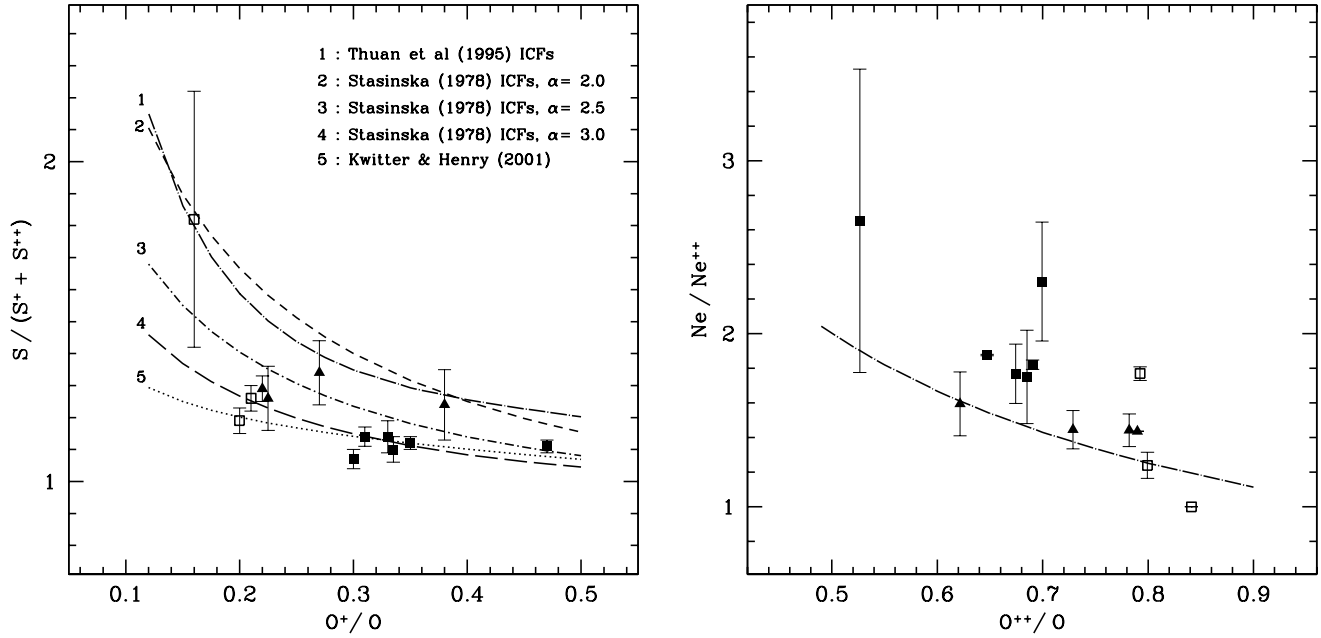

Fig. 4. The observed ratios $S/(S^+ + S^{++})$ and Ne/Ne^{++} compared with the theoretical ratios. The error bars show the extremes when using either the optical or infrared S^{++} and Ne^{++} ionic fraction. The objects N157B and N79A are not shown here. For an explanation of the symbols see Fig. 2.

[Ar IV] 4711 Å line. To get an estimate of the influence of the Ar^{+3} ionic fraction on the $\sum Ar^{+i}/Ar^{++}$ ratio, we derived it for 30 Dor#3. The [Ar IV] 4711 Å line flux in the optical spectra of 30 Dor#3 had a strength of 0.009 relative to Hβ. Using the electron temperature T_e [O III] and density n_e[S II] for this source this gave an Ar^{+3} ionic fraction of 2×10^{-7}. With this fraction, we arrived at an Ar^{+3}/Ar^{++}_{opt} ratio of ~0.17. The result of this little exercise clearly shows that the relative contribution of Ar^{+3} to the total Ar abundance can be significant. The warning issued in the previous paragraph is therefore warranted. On the other hand, it should be noted that the derived Ar^{+3} ionic fraction is an upper limit because the [Ar IV] 4711 Å line is blended with the He I 4713 Å line.

The results for the object N157B have not been included in this discussion about the ICFs. This is because the recipes for the ICFs are based on the assumption that the ionization structure within the source is in *photo*ionization equilibrium. The sample object N157B, however, is a supernova remnant and our line fluxes originate from a radiative shock. Our optical spectra of this object show clear evidence of shock enhancement. The ionization structure in a radiative shock is dominated by collisional processes and is not in equilibrium. The ICFs discussed here are therefore not applicable.

4.3.4. The full elemental abundances

In the derivation of the full elemental abundances the use of ICFs has been kept to a minimum. No ICF was used to derive the elemental abundance of oxygen, sulfur, helium and neon. The sulfur and neon abundances have been derived by simply summing the ionic fractions. Where optical and infrared ionic fractions are available for the same ion, their average has been used in the sum. For the derivation of the full abundance of nitrogen the ICF given in Eq. (7) is used, and for argon the one in Eq. (8) with $\alpha = 3.0$. The results are given in Table 3 together with abundances from the literature. In the case of N79A for which no infrared ionic fractions could be calculated, we also used ICFs for deriving the sulfur and neon abundances. We used the ICFs in Eqs. (6) and (8) with $\alpha = 3.0$, respectively. For N157B only the sum abundances are given because the standard ICFs cannot be applied in the case of an SNR (cf. Sect. 4.3.3).

A first look at Table 3 shows that within the two subsets of sources (SMC and LMC) the different abundances do not show much variation from source to source; the chemical composition of the sample is rather homogeneous. The nitrogen abundances for the positions in 30 Doradus, however, are lower than those for the other LMC sources. The difference in metallicity between the SMC and LMC is also clearly visible. The average abundances of the SMC are in general a factor 2 to 4 lower than those in the LMC. This is not the case for the helium abundance though which is basically constant throughout the entire sample. A few remarks must be made for some of the elemental abundances.

The oxygen abundance was derived with the assumption that the only two ionization stages of importance were O^+ and O^{++}. This assumption is quite safe because of the high ionization potential of O^{++} (~54 eV). The complete absence of He II recombination lines in our optical spectra shows that not many of these high-energy photons are present. The only object for which this assumption might lead to an underestimate of the oxygen abundance is N157B; the [O IV] 25.91 μm line has been detected for this object. The oxygen abundance found throughout the sample is lower than that quoted in the literature. This is mainly the result of the higher electron temperatures T_e [O III] derived in this work which lowers the abundance.

With the ionization potential of neutral sulfur at 10.4 eV and that of S^{+3} at 47.3 eV, the three ionic species S^{+}, S^{++} and S^{+3} contain most if not all of the sulfur within the H II region. The largest contributor to this abundance is S^{++}. Given the large ionization potential of S^{+3}, we estimate the possible contribution of S^{+4} to the total abundance to be not more than a few percent for the LMC sources. For the SMC sources, this contribution could be slightly larger given the high excitation of these sources ($O^{++}/O \simeq 0.80$). The high sulfur abundance of the object N159-9 is the result of the low T_e [S III] used in the derivation of the S^{++} ionic fraction. The sulfur abundances of N4A and N160A from Pagel et al. (1978) exceed the value found here by a factor of three. However, their sulfur abundance was derived by using the traditional ICF (O/O^{+}) which severely overestimates the missing sulfur.

Except for our sample objects N160A1 and A2, the argon abundance was derived by using an ICF. Our abundances agree well with the literature values, but for N81 our argon abundance is off by a factor of two when compared with the results from Heydari-Malayeri et al. (1988) and Pagel et al. (1978). These authors, however, assumed an argon ICF ≥ 2 which is quite likely too high (cf. Sect. 4.3.3).

No correction has been made for the possible presence of neutral helium. We think that given the high excitation of our sample sources ($0.53 < O^{++}/O < 0.84$) the contribution of the neutral species is negligible. Furthermore, all the optical spectra used in this study show He I 5875 / Hβ to be ~12 which indicates helium to be singly ionized throughout the H II region (e.g. Kennicutt et al. 2000).

For the uncertainty on the full elemental abundances we made the following estimates. The oxygen abundance is reliable within ~20%, and the uncertainty on the sulfur abundance is in the order of 40%. The case for neon is complicated because of the large uncertainties on the Ne^{++} ionic fraction and on the relative contribution of Ne^{+} to the total neon abundance. We assigned an uncertainty of at least 50% to the neon abundance. The uncertainty on the helium abundance is estimated to be $\leq$10%. For the abundance of argon and nitrogen the assessment of the uncertainty is more difficult because of the use of an ICF to derive them. The total error on these abundances stems from the error on the ionic fractions (N^{+}, Ar^{++}) and from the uncertainty in the O/O^{+} ratio used in the ICF. Given a typical error of ~20% on the O/O^{+} ratio and of 12% on the N^{+} ionic fraction the uncertainty on the nitrogen abundance is estimated to be 25%. The propagation of the errors on the Ar^{++} ionic fraction and on the O/O^{+} ratio through Eq. (8) yielded a typical uncertainty of ~20% on the total argon abundance.

5. The R23 and S23(4) abundance indicators

To derive reliable elemental abundances, a good determination of the electron temperature is needed. Other means of deriving abundances must be employed if no temperature can be derived. This is for example the case for H II regions in metal-rich galaxies where the [O III] 4363 Å line is seldom detected. The best known of these alternative methods is the so called "bright-line" method, where the bright emission lines from all the important ionization stages of an element are summed to get an estimate of its abundance. Examples of these are the R23 and S23 parameters for the oxygen and sulfur abundance, respectively (e.g. Pagel et al. 1979; Vílchez & Esteban 1996). The R23 parameter is defined as

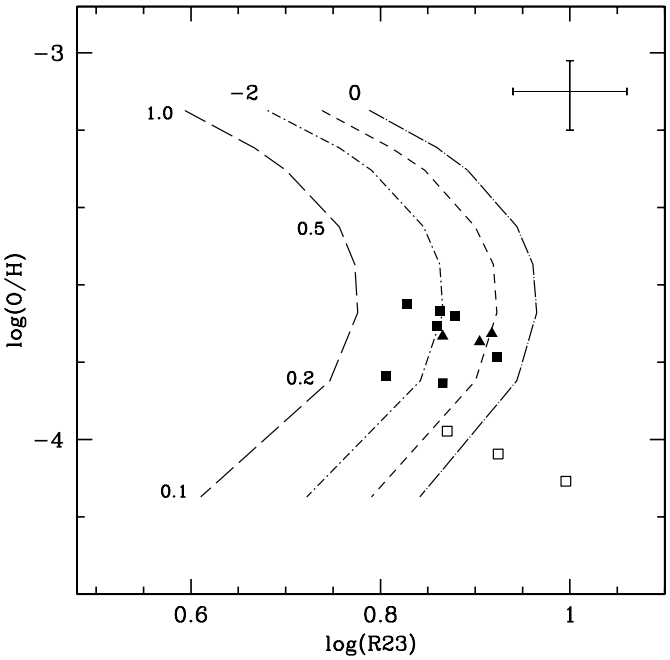

Fig. 5. The O abundance plotted against the R23 diagnostic. The model calculations for log $U = 0, -1, -2$ and -3 are shown. Shown in the upper right corner is a typical errorbar. For an explanation of the symbols see Fig. 2.

$$R23 = \frac{[O\,III]\,5007, 4959 + [O\,II]\,3727}{H\beta}, \tag{11}$$

and the S23 parameter as

$$S23 = \frac{[S\,III]\,9068, 9532 + [S\,II]\,6717, 6730}{H\beta}. \tag{12}$$

The link between the observed R23 and S23 parameters and the actual O and S abundances is usually provided by photoionization models.

Although the R23 and S23 parameters have proven themselves to be useful abundance indicators, they suffer from a few problems. The worst of these is the degenerate nature of the indicators, showing a low and a high-metallicity branch (see Fig. 5). This degeneracy can only be broken by invoking some other parameters like the [O III] 5007/[N II] 6583 ratio (Edmunds & Pagel 1984) for R23. In addition to this problem, the location of the inflection point of the parameter is poorly constrained, and the low-metallicity branch is very sensitive to changes in nebular parameters (especially U).

These problems with the R23 and S23 parameters have prompted several authors to calibrate the abundance indicators empirically (e.g. Dopita & Evans 1986; McGaugh 1991; Díaz & Pérez-Montero 2000). We do not have enough data points to perform such a calibration here but we can check the robustness of these parameters to the effects of incomplete spatial coverage of the objects and to variations in the spatial extent of

the observed objects. We therefore plot our oxygen and sulfur abundances against the R23 and S23 parameters as defined in Eqs. (11) and (12) in Fig. 5 and the lefthand panel of Fig. 6, respectively. We overplot our points with a small grid of general photoionization models, which was calculated using CLOUDY for a range of metallicities between 0.05 and 2.0 $Z_\odot$, and for the ionization parameters $\log U = -3, -2, -1$ and 0. The stellar atmosphere used was the D2 CoStar model from Schaerer & de Koter (1997). The hydrogen density was fixed at 500 cm^{-3} and the inner radius of the central cavity of the model was set at 10^{17} cm.

As can be seen in Fig. 5, our LMC sources lie in the turnabout region of the R23 relation which is located around $12 + \log(O/H) = 8.4$. All the LMC objects have about the same oxygen abundance (a bit lower for N79A and N159-5) and, within the uncertainties, also the same value for the R23 parameter. A similar good correspondence between the oxygen abundance and the R23 parameter is also found for our pointings in 30 Doradus. Given the fact that our spectra undersample this object spatially and that the different pointings in 30 Dor are spaced widely apart, this is encouraging. The case is less clear for our SMC sources though. The SMC object N66 falls between the model curves for $\log U = 0$ and -1, but although the oxygen abundance is lower, the object has about the same value for the R23 parameter as most of our LMC sources. The strong dependence of the low-metallicity branch of the R23 relation on the ionization parameter likely plays a role here. The SMC sources N81 and especially N88A deviate substantially from the model curves, but this is the result of the high [O III]/Hβ line ratio for these objects (see Paper I).

We might conclude that when looking at the LMC sources the R23 parameter seems to be robust to variations in spatial extent and coverage of the object. The uncertainties in the calibration of the low-metallicity branch of R23 and the exceptionally strong [O III] lines in the spectra of N81 and N88A, however, prevent us from extending this conclusion to the SMC sources. It should be mentioned that the different oxygen abundances and R23 parameters have been derived from a mix of stationary longslit and driftscan spectra.

The S23 parameter is, just like R23, doubly valued, but the turnabout point lies at a higher metallicity (~0.5 $Z_\odot$). The values of the S23 parameter for our sources plotted in the left panel of Fig. 6 show a similar picture as R23; there is a rough correspondence between a given value of S23 and the sulfur abundance. The conclusion as drawn for R23, however, is substantially less solid for S23 because of the much larger uncertainties on both the observed S23 parameter and the sulfur abundance. Note that the direction in which the ionization parameter increases for S23 is reversed when compared to the R23 parameter. Also note that the $\log U$ predicted by S23 is slightly higher than for the R23 parameter. Whether or not the low-metallicity branch of the S23 relation is less sensitive to the ionization parameter than R23 is stil unclear. We find it to be less sensitive for our models.

Because of the similar ionization potentials of O^+ and S^{++} it might be expected that S^{+3} plays an important role in the ionization balance. The S23 parameter has therefore been refined by including this ion in the expanded parameter S234 (Oey & Shields 2000). The new parameter S234 was defined as

$$\mathrm{S234} = \mathrm{S23} + \frac{[\mathrm{S\,IV}]\,10.5\,\mu\mathrm{m}}{\mathrm{H}\beta}, \tag{13}$$

including the [S IV] 10.5 μm line. A grid of generalized photoionization models calculated by Oey & Shields (2000) showed the S234 parameter to be very robust to changes in the ionization parameter U, which greatly enhances the usefulness of S234 as an abundance indicator. The lack of [S IV] 10.5 μm fluxes and of directly determined S^{+3} ionic fractions made it, however, difficult for these authors to check the reliability of the S234 parameter.

Our new sulfur abundances and the availability of the [S IV] 10.5 μm line in our data base allow such a check. The correlation between the sulfur abundances and the observed values for S234 is shown in the right panel of Fig. 6. Our analysis results agree well with the theoretical tracks. The insensitivity of the S234 parameter to changes in the ionization parameter as noted by Oey & Shields (2000) is confirmed by our models; for low metallicities, the different $\log U$ tracks almost completely overlap. For metallicities higher than about 0.5 $Z_\odot$, however, the models start to diverge. This is also roughly the location where the relation starts to bend back on itself. These results underline the usefulness and reliability of the newly proposed abundance indicator.

Given the tight overlap between the different $\log U$ curves we made a rough fit to the theoretical models. The following relation was found between log(S234) and log(S/H)

$$\log(\mathrm{S/H}) = -5.65 + 1.50\log(\mathrm{S234}). \tag{14}$$

The fit is plotted in the right panel of Fig. 6 (solid line). Our fit to the models is steeper and has its intercept at a somewhat lower sulfur abundance than the one found by Oey & Shields (2000). One should be cautious with the use of this relation for $\log(\mathrm{S234}) \geq 0.3$, because here the (S/H)−(S234) relations predicted by the various models start to diverge. Its use is therefore limited to metallicities lower than ~0.5 $Z_\odot$.

6. Nucleosynthetic aspects

Important constraints to stellar nucleosynthesis and to the star-formation history of a galaxy are provided by the ratio of the heavy element abundances to the oxygen abundance. The heavy element-to-oxygen ratios of elements like sulfur and neon provide information about the different rates at which these are produced in stars, whereas the nitrogen-to-oxygen ratio gives information about the initial mass function of generations of stars formed in the past (e.g. Henry & Worthey 1999). The heavy element-to-oxygen abundance ratios for sulfur, nitrogen, argon and neon for our sample objects are shown in Fig. 7. Also plotted in this figure are the values from Kobulnicky & Skillman (1996, 1997) and Izotov & Thuan (1999, IT99). The sample of IT99 consists of observations of giant H II regions in low-metallicity blue compact galaxies with oxygen abundances 12 + log(O/H) between 7.1 and 8.3. The Magellanic sources in the present work add to the high-metallicity end of this range.

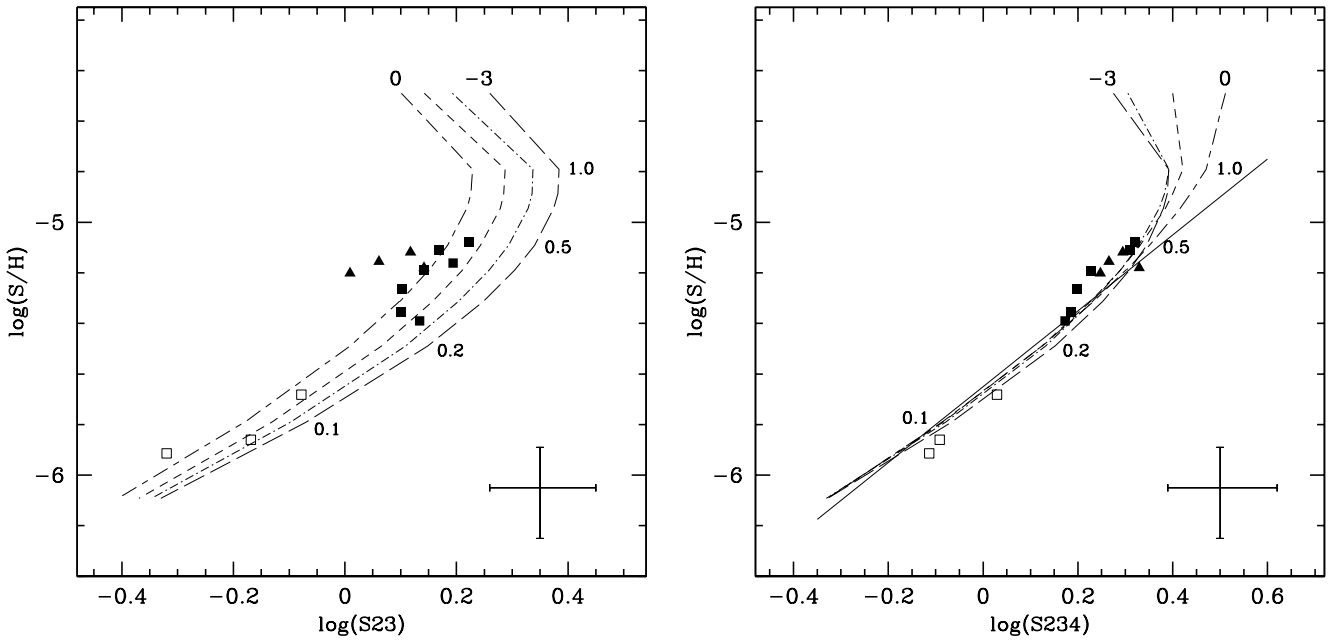

Fig. 6. The S abundance plotted against the S23 and S234 diagnostics, respectively. The model calculations for $\log U = 0, -1, -2$ and -3 are shown. The fit made to the models of S234 is shown as a solid line. Shown in the lower right corner is a typical errorbar. For an explanation of the symbols see Fig. 2.

All the heavy element-to-oxygen abundance ratios found for our sample are comparable to the ones in the literature. They show no dependency on the oxygen abundance which indicates the primary origin of the heavy elements. We find $\log\langle S/O\rangle = -1.48^{+0.14}_{-0.21}$ and $\log\langle Ar/O\rangle = -2.14^{+0.09}_{-0.12}$, which is very similar to the -1.55 ± 0.06 and -2.27 ± 0.10, respectively, found by IT99 for their high-metallicity subsample ($12 + \log(O/H) > 7.6$). Note that our Ar/O values are all at the high end of the distribution of values.

The $\log\langle Ne/O\rangle$ for our sources of $-0.52^{+0.15}_{-0.24}$ is higher than the -0.72 ± 0.06 found by IT99. However, the neon abundance derived for our sources is rather uncertain because of the sometimes large discrepancies between the infrared and optical Ne^{++} ionic fractions and of the suspiciously large relative contribution of Ne^{+} to the total neon abundance. This uncertainty is clearly seen in our Ne/O ratios which show a large scatter (see lower left panel of Fig. 7, upper half). In the derivation of the Ne/O abundance ratio both Kobulnicky & Skillman (1996, 1997) and IT99 use the equality $Ne^{++}/O^{++} = Ne/O$ (see also Eq. (6)). We can therefore test our suspicion by plotting our $Ne^{++}_{opt}/O^{++}_{opt}$ ratios together with the Ne/O ratios from these authors (lower left panel of Fig. 7, lower half). It is pretty obvious from this figure that the scatter is greatly reduced when compared to the upper half of the panel. The $\log\langle Ne^{++}_{opt}/O^{++}_{opt}\rangle$ is $-0.66^{+0.10}_{-0.12}$, in agreement with the $\log\langle Ne/O\rangle$ of IT99.

The evolution of nitrogen is still a subject of debate, not only because of the bimodal nature of the element (primary/secondary), but also because of the precise origin of the primary component of the total nitrogen abundance (IT99; Henry et al. 2000). The average N/O abundance ratio for the objects in our sample is $\log\langle N/O\rangle = -1.42^{+0.14}_{-0.20}$ (compare with IT99 -1.46 ± 0.14), and no correlation with the oxygen abundance is seen (see Fig. 7, lower left). This shows the nitrogen to be of mostly primary origin, which is in line with predictions that the contribution of secondary nitrogen to the total abundance is negligible for metallicities lower than $12 + \log(O/H) < 8.3$ (e.g. Shields et al. 1991).

Despite the fact that all our oxygen abundances for the LMC lie in a very narrow range we see some considerable scatter in the N/O ratio. Variations in the N/O ratio at a given metallicity have been established by several authors (e.g. Vila-Costas & Edmunds 1993; Marconi et al. 1994), but the underlying cause for this scatter is unsure. Pollution of the interstellar gas by W-R stars has been proposed as a mechanism for the observed local enhancements in the N/O ratio (Pagel et al. 1986), but Kobulnicky & Skillman (1998) oppose this view. The different time-scales in which nitrogen and oxygen are released into the interstellar medium also play an important role, but here things are unclear because of the question whether primary nitrogen is exclusively formed in intermediate-mass stars or is also produced in significant amounts in high-mass stars. Variations in the efficiency with which the newly produced nitrogen is dispersed through a galaxy and the possibility of differential outflow of nitrogen and oxygen add yet another layer of uncertainty. It is outside the scope of this paper to discuss which of these possible scenarios might be applicable to the LMC. Moreover, the uncertainties in our derived abundances are such that it is hard to say whether the scatter is really due to local enrichment.

7. Summary

Based on optical spectra and infrared data obtained with ISO-SWS/LWS, the temperature and density structure of a sample of Magellanic Cloud H II regions was determined. From this

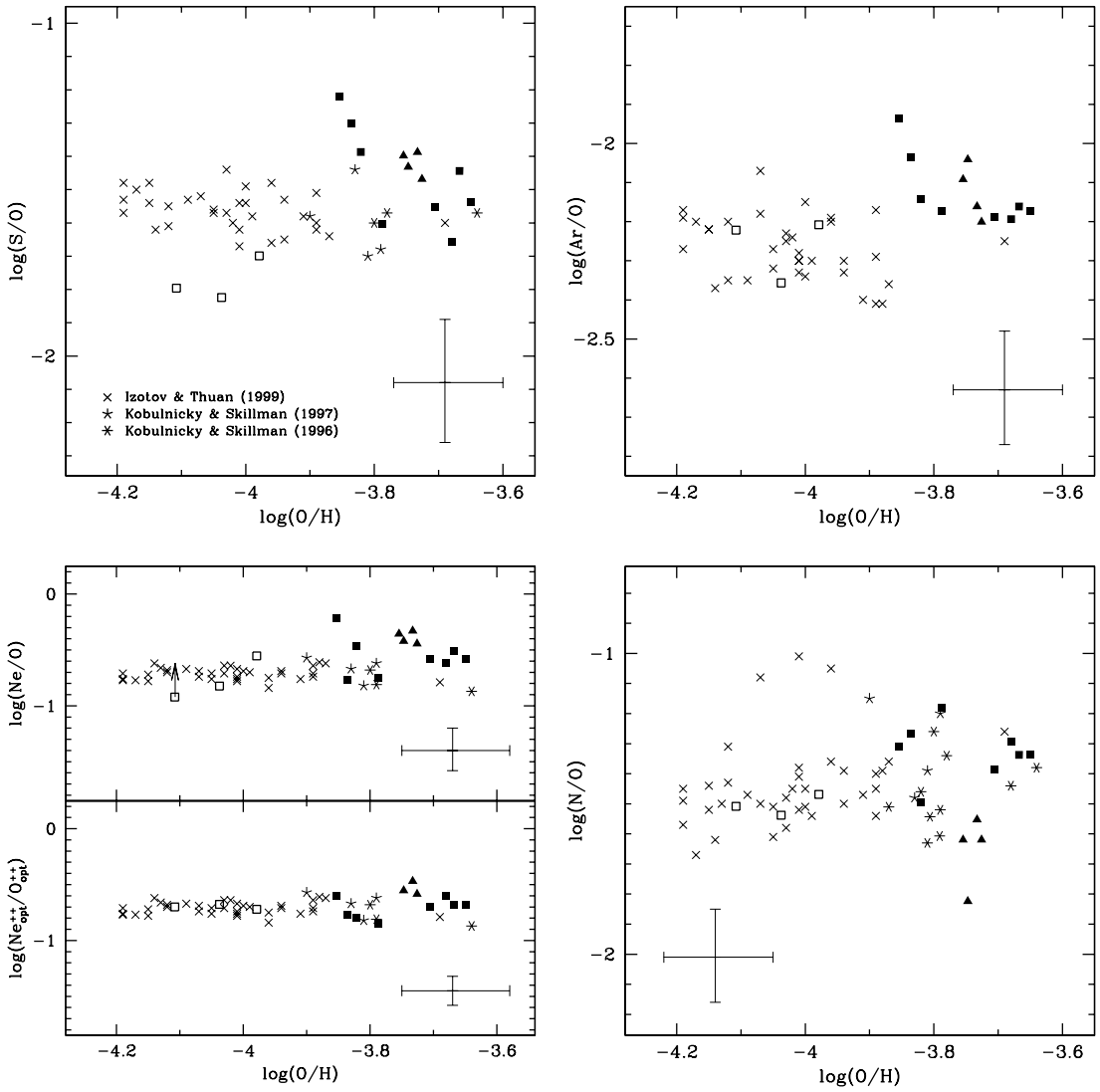

Fig. 7. The heavy element-to-oxygen abundance ratios S/O, Ar/O, Ne/O and N/O for our sample objects. Also shown in the lower left panel is the ($Ne^{++}_{opt}/O^{++}_{opt}$) ratio. In every panel a typical error bar is shown. For an explanation of the symbols designating the Magellanic sources see Fig. 2.

structure, new elemental abundances have been calculated for our sources.

The electron temperatures were derived for the O^+, O^{++} and S^{++} ionization zones from optical/optical line ratios. These were confronted with relations between the various temperatures from the literature. We conclude that the relation between T_e[O III] and T_e[O II] is fairly accurate. The relation between T_e[O III] and T_e[S III], however, might be slightly steeper. We therefore derived a new, empirical relation between these two temperatures. The issue of small-scale temperature fluctuations within an emitting zone (the t^2 problem) could not be addressed through optical/infrared line ratios because of the incompatibility of the optical and infrared line fluxes. Electron densities were derived for the same ionization zones as the temperatures using optical/optical and infrared/infrared line ratios. The derived densities for the different zones are all comparable, but suffer from the fact that the various fine-structure lines used in their derivation have been observed through various apertures.

Using these electron gas properties and our combined optical/infrared data base, we derived a new set of elemental abundances. Where possible, the individual ionic fractions were calculated with the electron gas properties of the corresponding ionization zone. An estimate of the uncertainties on the different ionic fractions is given. We compared the Ar^{++} and S^{++} ionic fractions as derived from the infrared and optical lines and found them to agree well. However, the infrared and optical Ne^{++} ionic fractions sometimes differ considerably. The full elemental abundances were calculated, when possible, without using ICFs. We compared the commonly used recipes for the sulfur and neon ICFs with the abundances derived from adding the different ionic fractions. We conclude that the sulfur ICF from Stasińska (1978) with $\alpha = 3$ is fairly accurate for $O^+/O > 0.2$. The validity of this ICF for $O^+/O < 0.2$ is less clear. Given the uncertainty in the neon abundance and the absence of an Ar^+ ionic fraction, no reliable comparison with the ICFs for neon and argon could be made.

We compared our spectra and the newly derived abundances with the bright-line abundance indicators R23 and S23(4). For this purpose, we computed a small grid of photoionization models. The small number of data points prevented us from calibrating these indicators empirically, but we checked their robustness for spatial undersampling of the sample objects and variations in their spatial extent. The [S IV] 10.5 μm line in our data base and the S^{+3} ionic fraction directly derived from this allowed us to check the newly proposed abundance indicator S234 empirically. The S234 data points from our sample agree well with the models, which show the S234 abundance indicator to be highly insensitive to the ionization parameter.

The heavy element-to-oxygen abundance ratios from our sources have been compared with those found for giant extragalactic H II regions in a large sample of low-metallicity blue compact galaxies (IT99). With our Magellanic Cloud sources we add to the high-metallicity end of this sample. Also included in the comparison are the results from Kobulnicky & Skillman (1996, 1997) for the irregular galaxies NGC 1569 and 4214. The average element-to-oxygen abundance ratios from our sources are comparable to the ones found in the literature and none of these shows any correlation with the oxygen abundance.

References

Benjamin, R. A., Skillman, E. D., & Smits, D. P. 1999, ApJ, 514, 307
Biemont, E., & Bromage, G. E. 1983, MNRAS, 205, 1085
Butler, K., & Zeippen, C. J. 1994, A&AS, 108, 1
Cai, W., & Pradhan, A. K. 1993, ApJS, 88, 329
Clegg, P. E., Ade, P. A. R., Armand, C., et al. 1996, A&A, 315, L38
de Graauw, Th., Haser, L. N., Beintema, D. A., et al. 1996, A&A, 315, L49
Dennefeld, M., & Stasińska, G. 1983, A&A, 118, 234
Díaz, A. I., & Pérez-Montero, E. 2000, MNRAS, 312, 130
Dopita, M. A., & Evans, I. N. 1986, ApJ, 307, 431
Edmunds, M. G., & Pagel, B. E. J. 1984, MNRAS, 211, 507
French, H. B. 1981, ApJ, 246, 434
Galavis, M. E., Mendoza, C., & Zeippen, C. J. 1995, A&AS, 111, 347
Galavis, M. E., Mendoza, C., & Zeippen, C. J. 1997, A&AS, 123, 159
Garnett, D. 1989, ApJ, 345, 282
Garnett, D. 1992, AJ, 103, 1330
Henry, R. B. C., & Worthey, G. 1999, PASP, 111, 919
Henry, R. B. C., Edmunds, M. G., & Köppen, J. 2000, ApJ, 541, 660
Heydari-Malayeri, M., & Testor, G. 1986, A&A, 162, 180
Heydari-Malayeri, M., Le Bertre, T., & Magain, P. 1988, A&A, 195, 230
Heydari-Malayeri, M., van Drom, E., & Leisy, P. 1990, A&A, 240, 481
Heydari-Malayeri, M., & Lecavelier des Etangs, A. 1994, A&A, 291, 960
Izotov, Y. I., & Thuan, T. X. 1999, ApJ, 511, 639
Kennicutt Jr., R. C., Bresolin, F., French, H., & Martin, P. 2000, ApJ, 537, 589
Kessler, M. F., Steinz, J. A., Anderegg, M. E., et al. 1996, A&A, 315, L27
Kobulnicky, H. A., & Skillman, E. D. 1996, ApJ, 471, 211
Kobulnicky, H. A., & Skillman, E. D. 1997, ApJ, 489, 636
Kobulnicky, H. A., & Skillman, E. D. 1998, ApJ, 497, 601
Kwitter, K. B., & Henry, R. B. C. 2001, ApJ, 562, 804
Lennon, D. J., & Burke, V. M. 1994, A&AS, 103, 273
Marconi, G., Matteucci, F., & Tosi, M. 1994, MNRAS, 270, 35
Mathis, J. S., Chu, Y.-H., & Peterson, D. E. 1985, ApJ, 292, 155
Mendoza, C. 1983, IAU Symp. 103, Planetary Nebulae, 143
Mendoza, C., & Zeippen, C. J. 1983, MNRAS, 202, 981
McGaugh, S. S. 1991, ApJ, 380, 140
McLauglin, B. M., & Bell, K. L. 1998, J. Phys. B, 31, 4317
Natta, A., Panagia, N., & Preite-Martinez, A. 1980, ApJ, 242, 596
Oey, M. S., & Shields, J. C. 2000, ApJ, 539, 687
Pagel, B. E. J., Edmunds, M. G., Fosbury, R. A. E., & Webster, B. L. 1978, MNRAS, 184, 569
Pagel, B. E. J., Edmunds, M. G., Blackwell, D. E., Chun, M. S., & Smith, G. 1979, MNRAS, 189, 95
Pagel, B. E. J., Terlevich, R. J., & Melnick, J. 1986, PASP, 98, 1005
Pagel, B. E. J., & Tautvaišienė, G. 1998, MNRAS, 299, 535
Pelan, J., & Berrington, K. A. 1995, A&AS, 110, 209
Peimbert, M. 1967, ApJ, 150, 825
Peimbert, M., & Costero, R. 1969, Bol. Obs. Tonantzintla y Tacubaya, 5, 3
Reed, B. C. 1989, AmJPh, 57, 642
Rosa, M., & Mathis, J. S. 1987, ApJ, 317, 163
Russell, S. C., & Dopita, M. A. 1992, ApJ, 384, 508
Saraph, H. E., & Tully, J. A. 1994, A&AS, 107, 29
Saraph, H. E., & Storey, P. J. 1999, A&AS, 134, 369
Schaerer, D., & de Koter, A. 1997, A&A, 322, 598
Shaver, P. A., McGee, R. X., Newton, L. M., Danks, A. C. & Pottasch, S. R. 1983, MNRAS, 204, 53
Shields, G. A., Skillman, E. D., & Kennicutt, R. C. 1991, ApJ, 371, 82
Stasińska, G. 1978, A&A, 66, 257
Storey, P. J., & Hummer, D. G. 1995, MNRAS, 272, 41
Testor, G., & Pakull, M. 1985, A&A, 145, 170
Tsujimoto, T., Nomoto, K., Yoshii, Y., et al. 1995, MNRAS, 277, 945
Thuan, T. X., Izotov, Y. I., & Lipovetsky, V. A. 1995, ApJ, 445, 108
Vila-Costas, M. B., & Edmunds, M. G. 1993, MNRAS, 265, 199
Vílchez, J. M., & Esteban, C. 1996, MNRAS, 280, 720
Vermeij, R., Damour, F., van der Hulst, J. M., & Baluteau, J.-P. 2001, A&A, 390, 649 (Paper I)